Supporting Information

Seven-photon absorption from Na^{+}/Bi^{3+}-alloyed $Cs_2AgInCl_6$ perovskites

Shiling Jin,[1, +] Renfu Li,[2, +] Jiwen Zhu,[1] Tao Pang [3], Tianmin Wu,[4, *] Hongbing Zhan,[5] Yuanhui Zheng,[6, 7] Feng Huang,[1] Xueyuan Chen,[2, *] Daqin Chen [1, 6, 8, *]

[1] College of Physics and Energy, Fujian Normal University, Fujian Provincial Key Laboratory of Quantum Manipulation and New Energy Materials, Fuzhou, Fujian 350117, China
E-Mail: dqchen@fjnu.edu.cn (D. Q. Chen)

[2] CAS Key Laboratory of Design and Assembly of Functional Nanostructures, Fujian Key Laboratory of Nanomaterials and State Key Laboratory of Structural Chemistry, Fujian Institute of Research on the Structure of Matter, Chinese Academy of Sciences, Fuzhou, Fujian 350002, China
E-Mail: xchen@fjirsm.ac.cn (X. Y. Chen)

[3] Huzhou Key Laboratory of Materials for Energy Conversion and Storage, College of Science, Huzhou University, Zhejiang, Huzhou 313000, China

[4] College of Photonic and Electronic Engineering, Fujian Normal University, Fuzhou, Fujian 350117, China
E-Mail: wtm@fjnu.edu.cn (T. M. Wu)

[5] College of Materials Science and Engineering, Fuzhou University, Fuzhou, Fujian 350108, China

[6] Fujian Science & Technology Innovation Laboratory for Optoelectronic Information, Fuzhou, Fujian 350116, China

[7] College of Chemistry, Fuzhou University, Fuzhou, Fujian 350116, China

[8] Fujian Provincial Collaborative Innovation Center for Advanced High-Field Superconducting Materials and Engineering, Fuzhou, Fujian 350117, China

[+]S. L. Jin and R. F. Li contributed equally.

Table S1. The comparison of DPs with a series of conventional perovskites, including structure, PLQY, pulse condition, excitation wavelength, bandgap type and mechanism. NCs, NPs, MCs, and SC represent nanocrystals, nanoplatelets, microcrystals and single crystal respectively. 0D, 2D, and 3D represent 0-dimensional, 2-dimensional, and 3-dimensional.

Composition	**Structure**	**PLQY**	**Pulse condition**	**Excitation wavelength**	**Bandgap energy (eV)**	**Mechanism**	**Ref.**
$Cs_2Na_{0.4}Ag_{0.6}In_{0.99}Bi_{0.01}Cl_6$	**3D MCs**	**98.82%**	**120 fs, 1 kHz**	**800-2600 nm**	**3.17**	**2-7 PA**	**this work**
$CsPbBr_3$	3D NCs	55%	50 fs, 1 kHz	675-2300 nm	2.40	2-5 PA	S1
$CsPbBr_3$	3D NCs	-	15 ps, 78 MHz	700-1030 nm	2.37	2-4 PA	S2
$CsPbCl_3$	3D MCs	-	50 fs, 1 kHz	800-2200 nm	3.50	2-6 PA	S3
Cs_4PbBr_6	0D NCs	-	70 fs, 1 kHz	500-1500 nm	4.00	2-4 PA	S4
$CsPbBr_{2.7}I_{0.3}$	2D NPs	3.1%, 7.6%	100 fs	800-2200 nm	2.36, 2.65	2-5 PA	S5
$CH_3NH_3PbBr_3$	3D SC	-	100fs	800 nm	2.21	2 PA	S6
$MAPbBr_3$	3D NCs	84%	-	-	2.36	2-5 PA	S1
Mn-doped $CsPbCl_3$	3D NCs	-	120 fs, 1 kHz	720	3.55	2 PA	S7
$MAPbBr_3/(OA)_2PbBr_4$	NCs	92%	50 fs, 1 kHz	675-2300 nm	-	2-5 PA	S1

Table S2. Elemental percentage (mol%) in the $Cs_2Na_{0.4}Ag_{0.6}In_{0.90}Bi_{0.10}Cl_6$ sample determined from EDX data.

Element	Cs	Na	Ag	In	Bi	Cl
mol%	20.39	1.83	4.51	7.15	2.08	64.04

Table S3. The comparison of dopant concentrations obtained from ICP-MS data for the $Cs_2Na_{0.4}Ag_{0.6}In_{1-x}Bi_xCl_6$ (x=0.05, 0.10, 0.40, 0.60, 0.80) products. The nominal ratio and the actual doping content are determined based on the equation of [Bi]/[Bi+In].

Materials	Nominal ratio	Actual content (ICP-MS)
$\mathbf{Cs_2Na_{0.4}Ag_{0.6}In_{0.95}Bi_{0.05}Cl_6}$	5%	6.45%
$\mathbf{Cs_2Na_{0.4}Ag_{0.6}In_{0.90}Bi_{0.10}Cl_6}$	10%	14.94%
$\mathbf{Cs_2Na_{0.4}Ag_{0.6}In_{0.60}Bi_{0.40}Cl_6}$	40%	49.54%
$\mathbf{Cs_2Na_{0.4}Ag_{0.6}In_{0.40}Bi_{0.60}Cl_6}$	60%	72.04%
$\mathbf{Cs_2Na_{0.4}Ag_{0.6}In_{0.20}Bi_{0.80}Cl_6}$	80%	86.29%

Table S4. Optical properties for the $Cs_2Na_{0.4}Ag_{0.6}In_{1-x}Bi_xCl_6$ (x=0~1) samples, including excitation wavelength (λ_{ex}), peak position, photoluminescence maximum (PL_{max}), full width at half maxima (FWHM), integrated intensity, and PLQY data.

$Cs_2Na_{0.4}Ag_{0.6}In_{1-x}Bi_xCl_6$ (x)	0	0.01	0.05	0.10	0.20	0.40	0.60	0.80	1.00
λ_{ex} (nm)	289	365	365	337	333	333	376	365	333
Peak position (nm)	595	603	612	620	635	650	645	642	634
PL_{max}	9509	110399	109144	83937	50050	18512	12755	3190	3710
FWHM (nm)	185	195	197	201	206	210	211	216	218
Integrated intensity	2013403	23618811	23137981	18201315	11179503	4142314	2887725	728987	847143
PLQY	19.54%	**98.82%**	**96.14%**	75.80%	55.41%	30.38%	5.66%	2.46%	4.20%

Table S5. Comparison of 2-photon absorption cross-section (σ_2) and nonlinear absorption coefficient (β) of DP with organic chromophores and conventional semiconductors.

Materials	Measured condition	Nonlinear optical parameters		Refs.
		β (cm GW^{-1})	σ_2 (GM)	
π-Delocalizable Metallodendrimers	810 nm; 130 fs; 1 kHz	—	370	S8
1,4-Bis(carbazolyl)benzene derivatives	720 nm; 100 fs; 80 MHz	—	448	S9
Diphenylamino and 1,2,4-triazole	800 nm; 100 fs; 1 kHz	—	57	S10
CdSe NCs (2.4 nm)	840 nm; 100 fs; 82 MHz	—	390	S11
CdS NCs (4.6 nm)	800 nm; 100fs; 80 MHz	—	200	S12
$Cs_3Cu_2I_5$ SCs	600 nm; 100 fs; 1 kHz	5.10×10^{-3}	—	S13
$CsCu_2I_3$ SCs	600 nm; 100 fs; 1 kHz	2.10×10^{-1}	—	S13
$CH_3NH_3PbBr_3$ SCs	1000 nm; 70 fs; 1 kHz	5.20	—	S14
$C_6H_5CH_2NH_3PbBr_3$ film	800 nm; 68 fs	1.83×10^{-3}	—	S15
InP/ZnS NCs (3.5 nm)	803 nm; 130 fs; 1 kHz	—	260	S16
$CsPbCl_3$ MCs (1-5 μm)	800 nm; 50 fs; 1 kHz	3.80	—	S2
$MAPbBr_3$ NCs (15 nm)	800 nm	4.20×10^{-3}	—	S17
$Cs_2Na_{0.4}Ag_{0.6}In_{0.99}Bi_{0.01}Cl_6$ NCs	**800 nm; 120 fs; 1 kHz**	**1.21×10^{-1}**	**485**	**This work**

Table S6. The fitted lifetimes of $Cs_2Na_{0.4}Ag_{0.6}In_{0.99}Bi_{0.01}Cl_6$ DP upon various fs laser excitation wavelengths.

Excitation wavelength	A_1	τ_1	A_2	τ_2	τ_{ave}
365 nm	1890	2.48	590	5.24	3.58
810 nm	1764	1.47	599	5.85	3.99
900 nm	1830	1.77	383	7.46	4.44
950 nm	1621	1.55	470	6.25	4.08
1000 nm	2021	2.31	357	7.15	4.02
1100 nm	1898	2.18	395	7.04	4.13
1200 nm	1812	1.89	405	7.35	4.43
1300 nm	1697	1.75	424	7.60	4.79
1400 nm	1677	1.62	476	7.33	4.83
1500 nm	1923	1.25	584	5.91	4.00
1600 nm	1944	1.10	747	5.19	3.74
1700 nm	2049	0.83	859	4.21	3.13
1800 nm	1628	0.89	653	4.76	3.53
1900 nm	1867	0.82	892	4.44	3.43
2000 nm	2293	0.99	851	4.84	3.47
2100 nm	2225	1.28	672	6.16	4.17
2200 nm	1904	1.29	688	5.87	4.14
2300 nm	2064	1.08	776	5.23	3.76
2400 nm	2311	0.83	919	4.52	3.36
2500 nm	2129	1.14	793	5.44	3.89
2600 nm	2222	1.45	642	6.60	4.37

Table S7. The evaluated single- and multi-photon excited decay lifetimes for the $Cs_2Na_{0.4}Ag_{0.6}In_{0.99}Bi_{0.01}Cl_6$ DP under 365 nm, 950 nm, and 1400 nm laser excitation recorded at different temperatures (10~300 K).

T (K)	10	50	90	130	170	210	250	270	300
τ_{365} (μs)	9.55	11.37	11.32	11.08	10.15	8.22	5.96	4.42	3.22
τ_{950} (μs)	55.60	54.61	53.02	47.05	54.10	48.36	24.13	10.63	3.75
τ_{1400} (μs)	47.38	48.47	46.06	46.25	57.87	56.24	17.06	11.47	5.50

Herein, PL decay curves are fitted by a two-exponential function of $I(t) = A_1\exp\left(\frac{-t}{\tau_1}\right) + A_2 exp(\frac{-t}{\tau_2})$, where A_1 and A_2 denote the corresponding amplitudes of two lifetime components τ_1 and τ_2. Notably, these two lifetime components have not any physical meanings, and this equation is just used to determine the average lifetime using the following equation of $\tau_{ave} = \frac{A_1\tau_1^2 + A_2\tau_2^2}{A_1\tau_1 + A_2\tau_2}$.

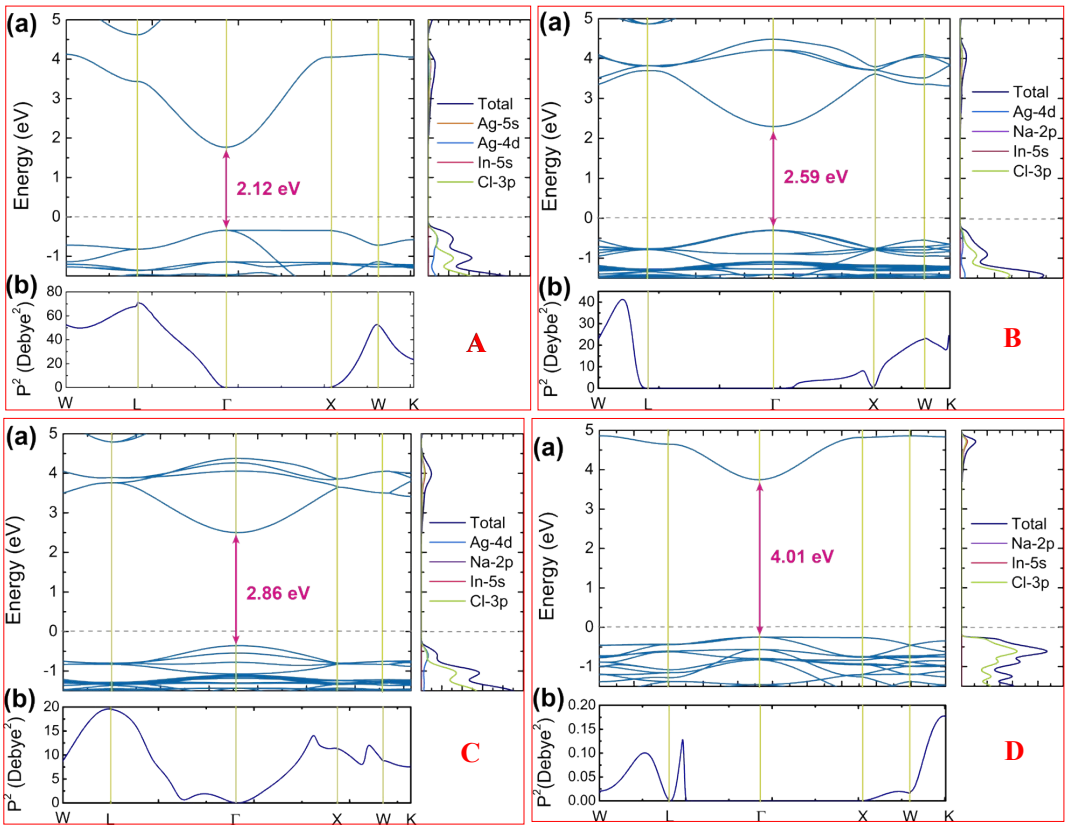

Figure S1. DFT-calculated electronic band structure, PDOS and TDME for (A) the $Cs_2AgInCl_6$, (B) $Cs_2Na_{0.25}Ag_{0.75}InCl_6$, (C) $Cs_2Na_{0.4}Ag_{0.6}InCl_6$, and (D) $Cs_2NaInCl_6$ DPs.

Note S1: An electronic band structure of $Cs_2AgInCl_6$ calculated via DFT with HSE06 hybrid functional shows that $Cs_2AgInCl_6$ possesses a direct band gap with both valance band maximum (VBM) and conduction band minimum (CBM) at the Γ high symmetry point, and the calculated electronic band gap (~2.12 eV) is well consistent with previous theoretical study. Projected density of states (PDOS) analysis reveals that the bottom of conduction band mainly derives from the delocalized In-*5s*, Cl-*3p* and Ag-*5s* orbitals, while the top of the valence band is mainly comprised of Cl-*3p* and Ag-*4d* orbitals. Due to parity-forbidden transition originated from the centro-symmetry of $Cs_2AgInCl_6$ and the lowest conduction band derived from the unoccupied In-*5s* orbitals,[S18] the calculated electronic band gap here is considerably smaller than the experimental observed optical band gap (3.54 eV). The calculated transition dipole matrix elements (TDMEs) are zero at the Γ point and along the Γ-X direction, clearly shows a parity-forbidden transition from VBM to CBM.

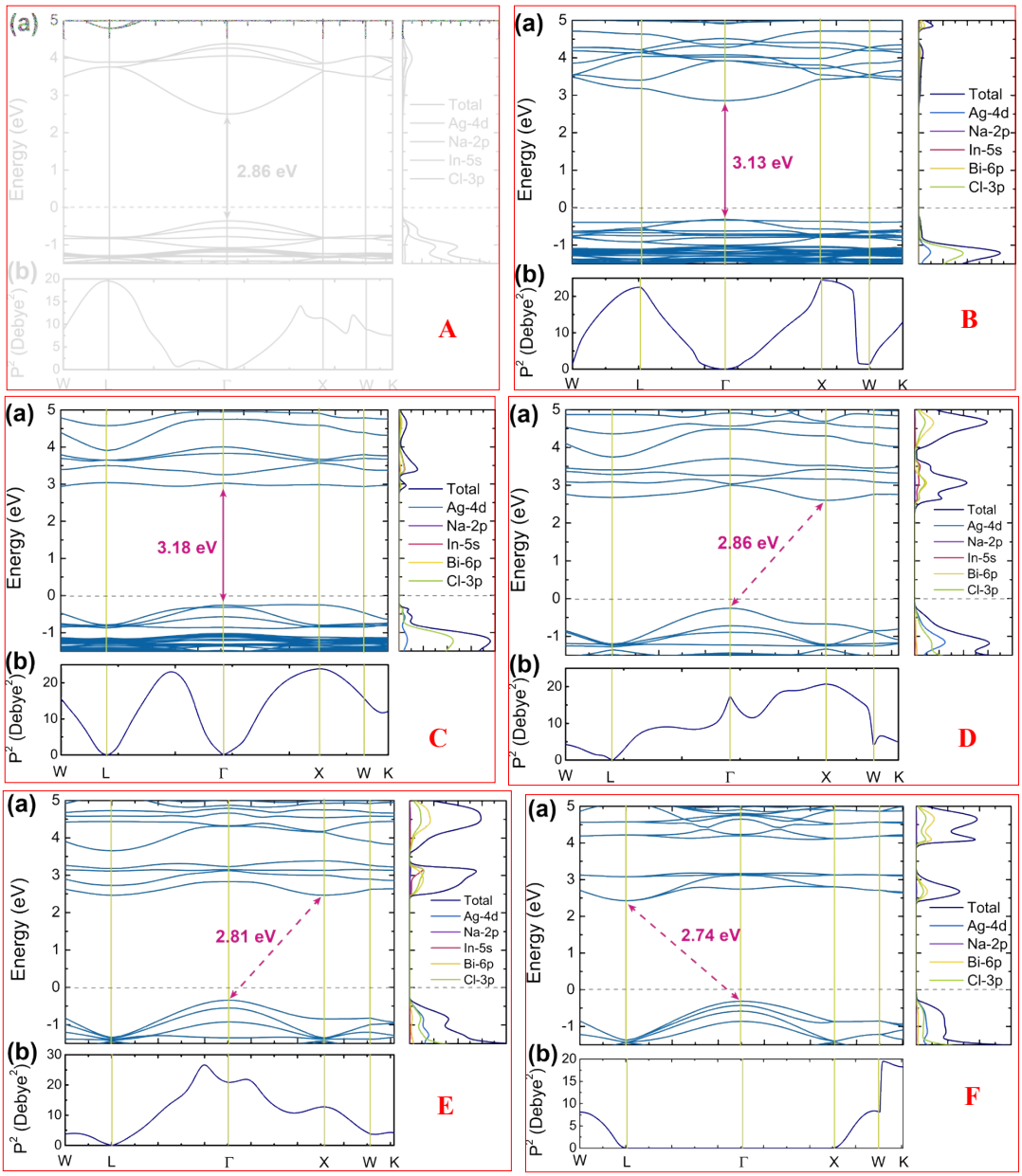

Figure S2. DFT-calculated electronic band structure, PDOS and TDME for (A) $Cs_2Na_{0.4}Ag_{0.6}InCl_6$, (B) $Cs_2Na_{0.4}Ag_{0.6}In_{0.875}Bi_{0.125}Cl_6$, (C) $Cs_2Na_{0.4}Ag_{0.6}In_{0.75}Bi_{0.25}Cl_6$, (D) $Cs_2Na_{0.4}Ag_{0.6}In_{0.5}Bi_{0.5}Cl_6$, (E) $Cs_2Na_{0.4}Ag_{0.6}In_{0.25}Bi_{0.75}Cl_6$, and (F) $Cs_2Na_{0.4}Ag_{0.6}BiCl_6$ DPs.

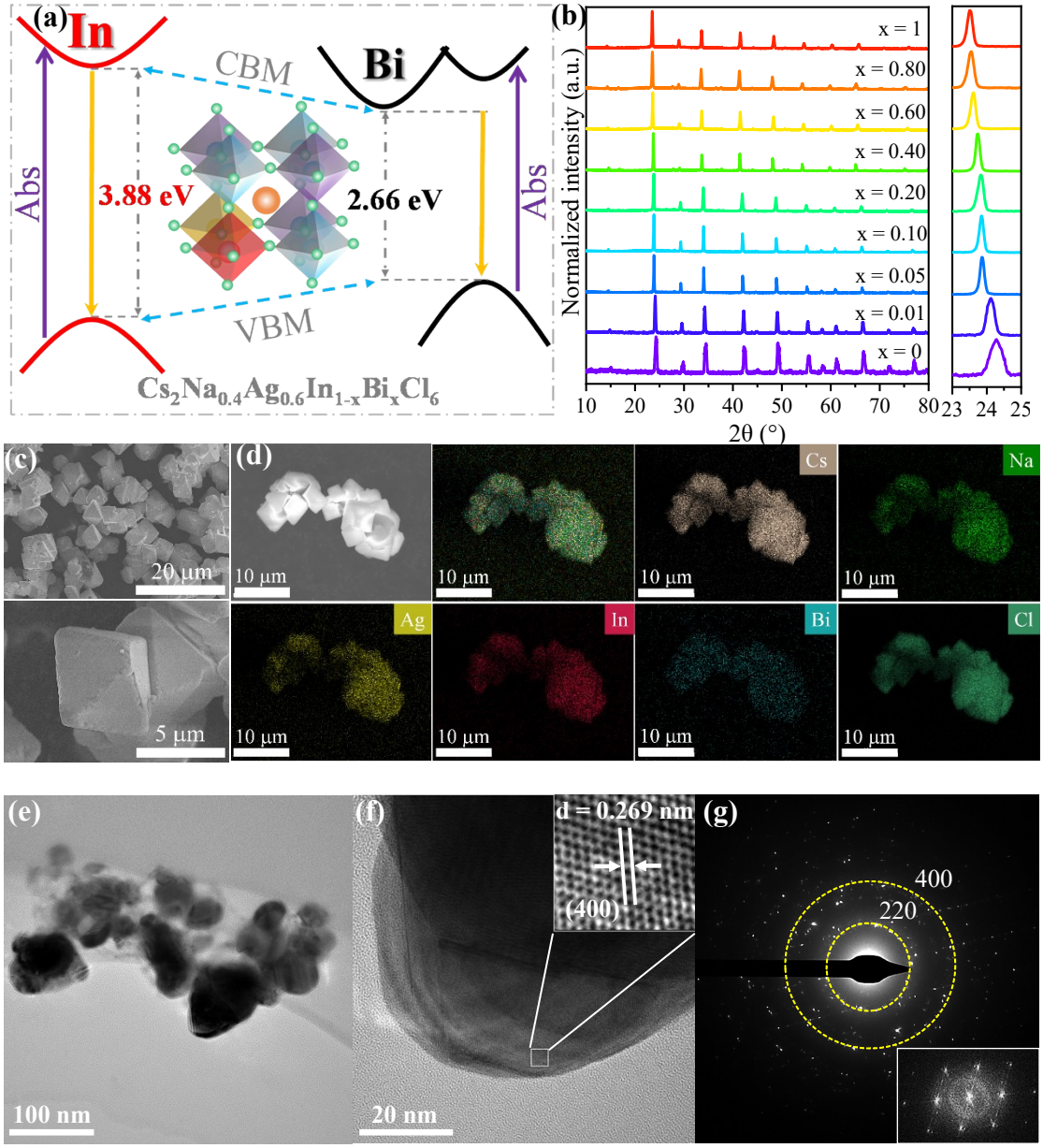

Figure S3. **(a)** Crystal structure of $Cs_2Na_{0.4}Ag_{0.6}In_{1-x}Bi_xCl_6$. **(b)** XRD patterns of $Cs_2Na_{0.4}Ag_{0.6}In_{1-x}Bi_xCl_6$ (x=0~1) MCs and the magnified XRD patterns in the region of 22° ~ 25°. **(c)** SEM images of a typical $Cs_2Na_{0.4}Ag_{0.6}In_{0.90}Bi_{0.10}Cl_6$ sample and **(d)** EDX elemental mappings showing the distribution of Cs, Na, Ag, In, Bi and Cl in the MCs. **(e)** TEM image, **(f)** High-resolution TEM image and **(g)** the corresponding SAED pattern of $Cs_2Na_{0.4}Ag_{0.6}In_{0.90}Bi_{0.10}Cl_6$ MCs. The inset shows the fast Fourier transform (FFT) pattern.

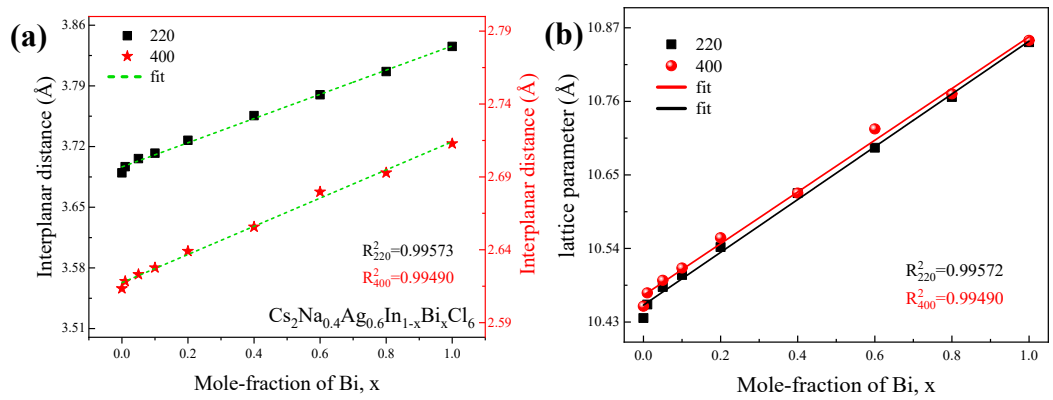

Figure S4. Dependence of interplanar distances and lattice parameters determined from (220) and (400) diffraction peaks on the Bi^{3+} content. Obviously, a monotonic increase trend is observed with increase of Bi^{3+} content.

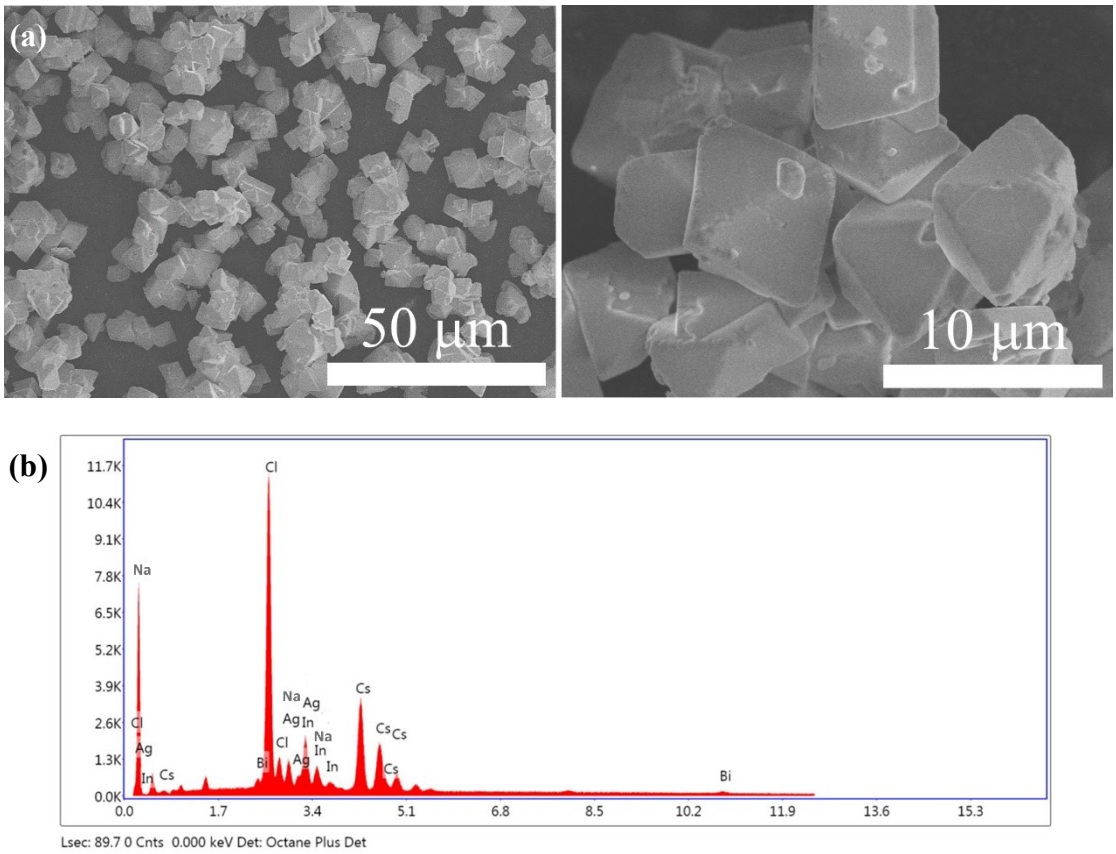

Figure S5. (a) SEM images of a typical $Cs_2Na_{0.4}Ag_{0.6}In_{0.90}Bi_{0.10}Cl_6$ sample. (b) EDX spectrum recorded from the $Cs_2Na_{0.4}Ag_{0.6}In_{0.90}Bi_{0.10}Cl_6$ sample, showing the existence of Cs, Na, Ag, Bi, In, Cl elemental signals.

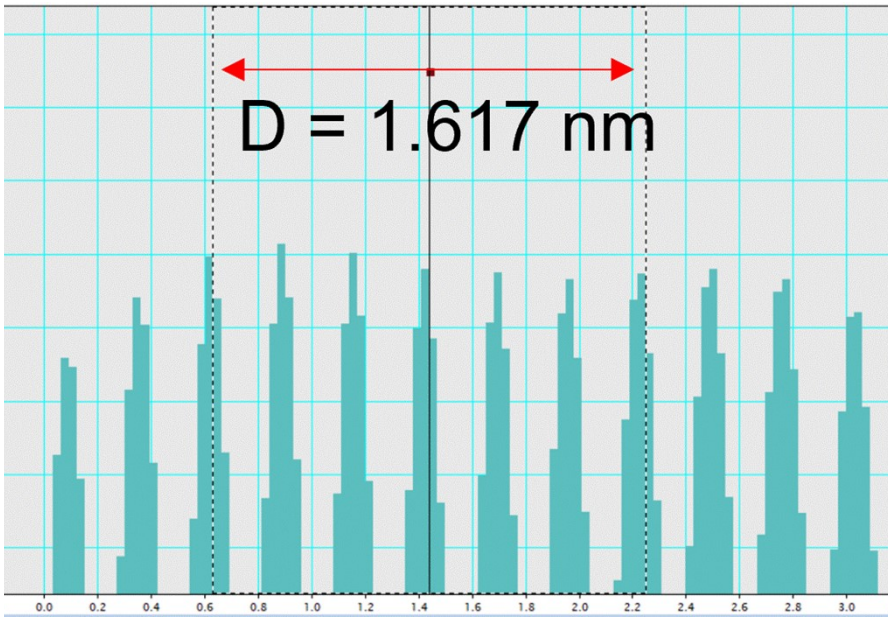

Figure S6. The distance of the six lattice planes in the direction of the (400) diffraction peak is determined to be 1.617 nm.

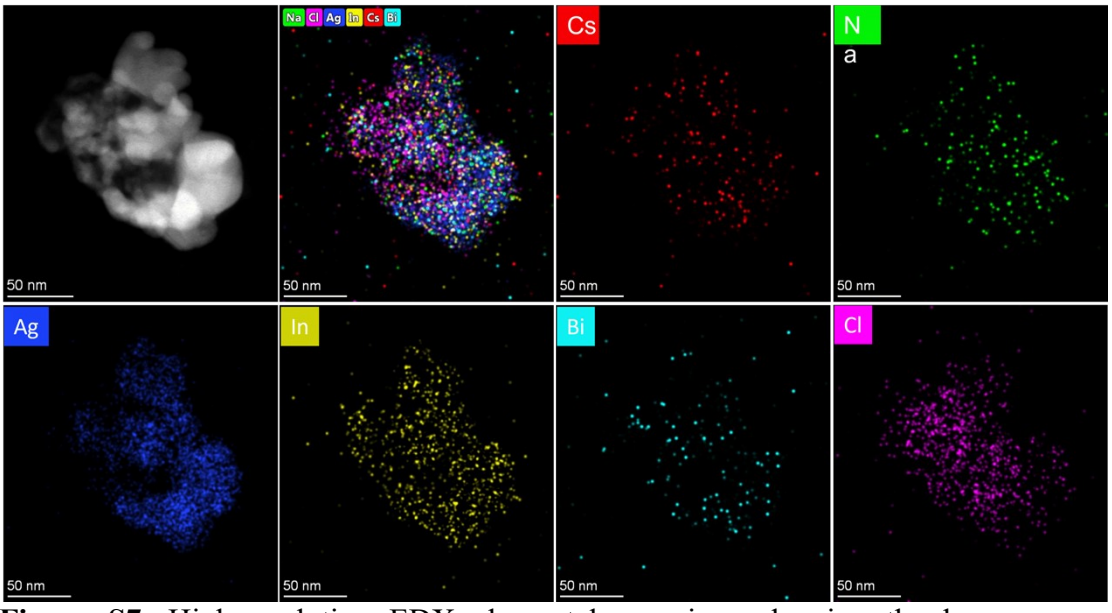

Figure S7. High-resolution EDX elemental mappings showing the homogenous distribution of Cs, Na, Ag, In, Bi and Cl signals in the $Cs_2Na_{0.4}Ag_{0.6}In_{0.90}Bi_{0.10}Cl_6$ MCs.

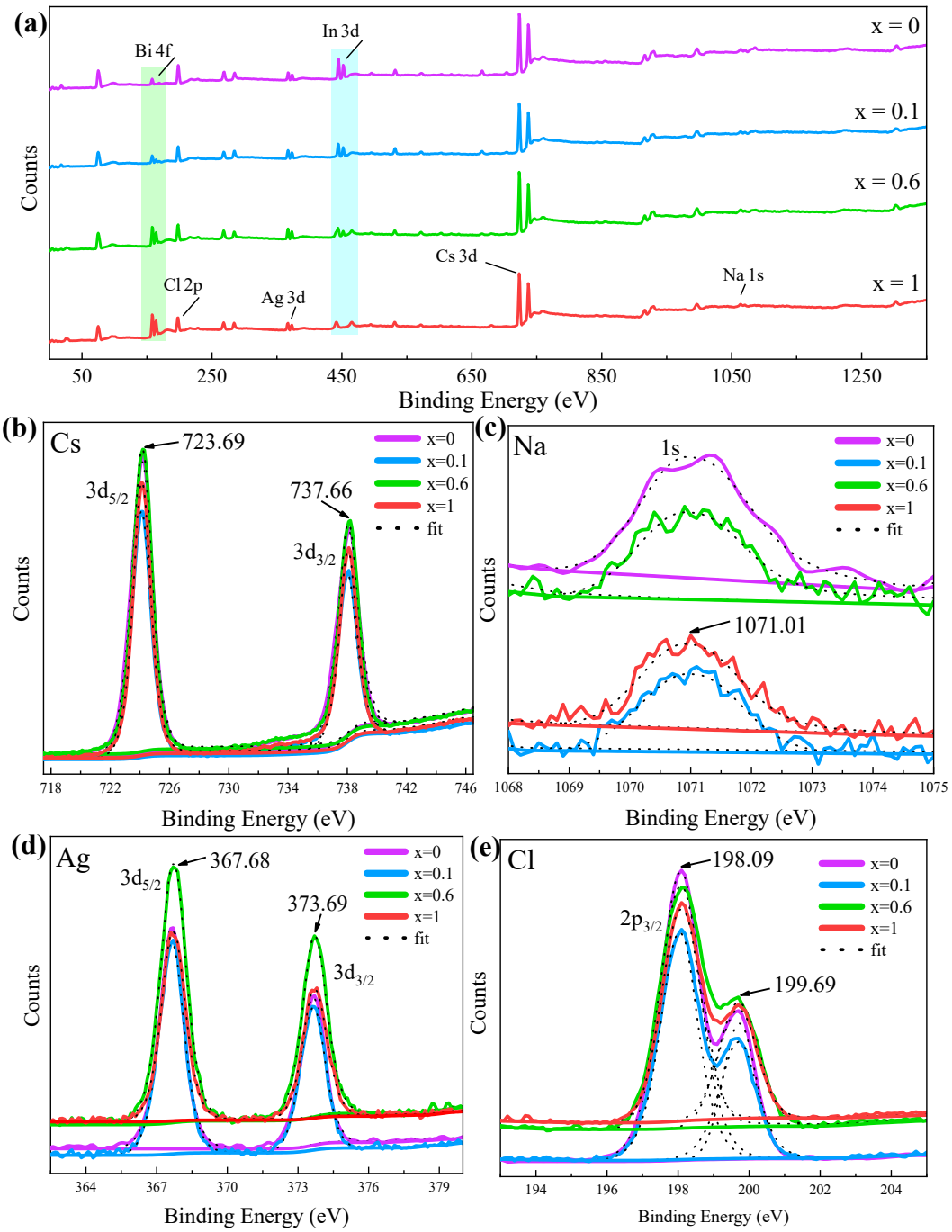

Figure S8. X-ray photoelectron spectra of (a) all the elements, (b) Cs 3d, (c) Na 1s, (d) Ag 3d and (e) Cl 2p for the as-prepared $Cs_2Na_{0.4}Ag_{0.6}InCl_6$, $Cs_2Na_{0.4}Ag_{0.6}In_{0.90}Bi_{0.10}Cl_6$, $Cs_2Na_{0.4}Ag_{0.6}In_{0.40}Bi_{0.60}Cl_6$ and $Cs_2Na_{0.4}Ag_{0.6}BiCl_6$ samples.

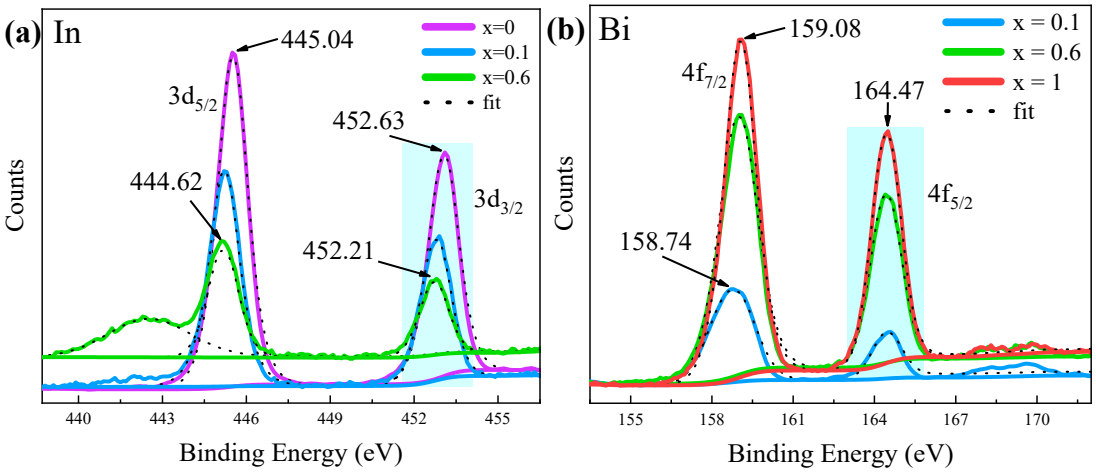

Figure S9. X-ray photoelectron spectra of (a) In 3d and (b) Bi 4f for the $Cs_2Na_{0.4}Ag_{0.6}InCl_6$, $Cs_2Na_{0.4}Ag_{0.6}In_{0.90}Bi_{0.10}Cl_6$, $Cs_2Na_{0.4}Ag_{0.6}In_{0.40}Bi_{0.60}Cl_6$ and $Cs_2Na_{0.4}Ag_{0.6}BiCl_6$ samples.

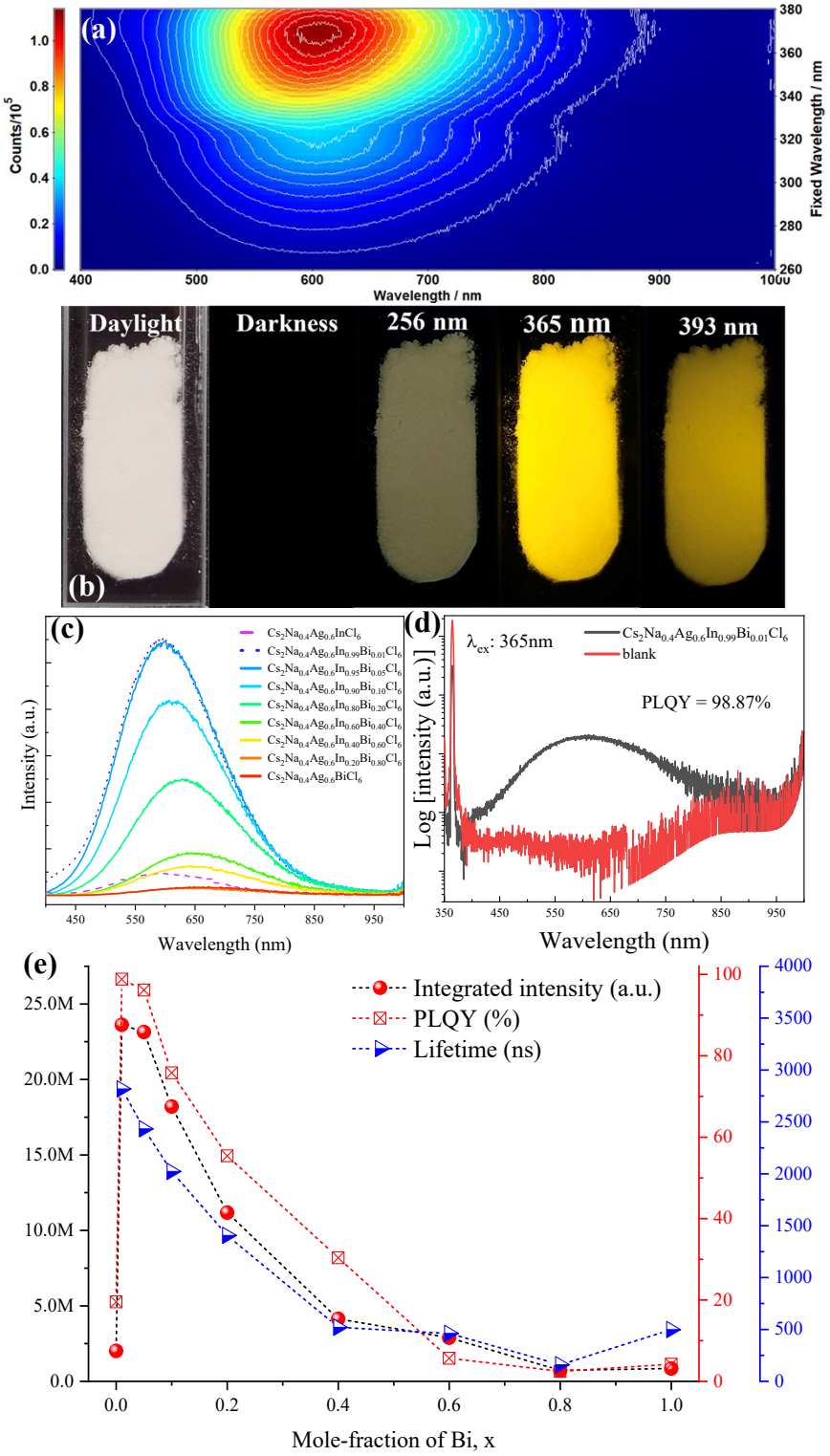

Figure S10. (a) Contour plot of the $Cs_2Na_{0.4}Ag_{0.6}In_{0.99}Bi_{0.01}Cl_6$ sample, showing dependence of PL on the excitation wavelength in the range of 260-380 nm. (b) Photographs of the sample under daylight, darkness, 256 nm, 365 nm and 393 nm UV light excitations. (c) PL spectra (λ_{ex}=365 nm) of the $Cs_2Na_{0.4}Ag_{0.6}In_{1-x}Bi_xCl_6$ samples. (d) Quantitative PL spectra of the $Cs_2Na_{0.4}Ag_{0.6}In_{0.99}Bi_{0.01}Cl_6$ and the reference to

determine PLQY. (e) Dependence of PL integrated intensity, PLQY, and decay lifetime on Bi concentration.

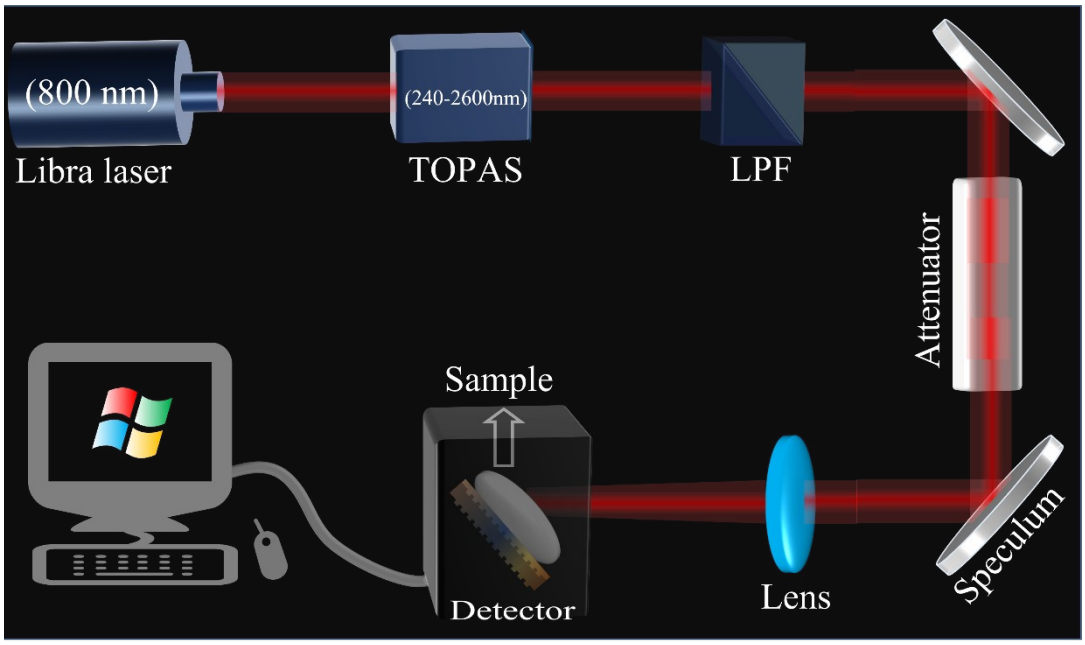

Figure S11. For MPA-upconverted experiments, the excitation pulse (1 kHz, 240-2,600 nm, pulse width ,120 fs) was generated by an optical parametric amplifier (TOPAS-F-UV2, Spectra-Physics) pumped by a regeneratively amplified femtosecond Ti: sapphire laser system (800 nm, 1 kHz, pulse energy 4 mJ, pulse width, 120 fs, Spitfire Pro-F1KXP, Spectra-Physics), which was seeded by a femtosecond Ti-sapphire oscillator (80 MHz, pulse width ,70 fs, 710-920 nm, Maitai XF-1, Spectra-Physics). Notably, LPF represents long-pass filter.

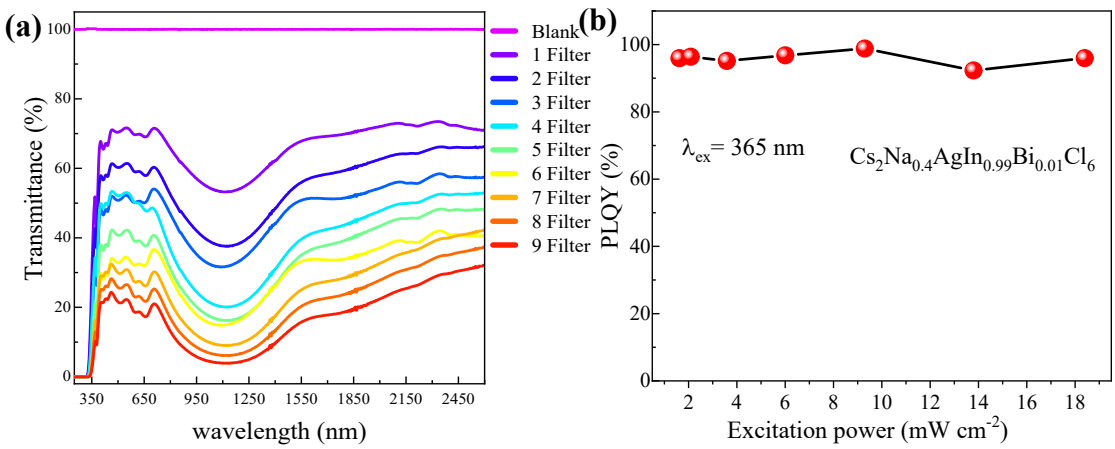

Figure S12. (a) The correlated transmittance of attenuation sheets 1 - 9, where the blank is for the case without the attenuation sheet (the variable power calculated in this way is more accurate than the direct reading of the power value). (b) PLQY of $Cs_2Na_{0.4}Ag_{0.6}In_{0.99}Bi_{0.01}Cl_6$ versus excitation power, showing no obvious change of PLQY with increase of excitation powers. This result indicates that the variation of excitation power is not directly related to the PLQY of the sample.

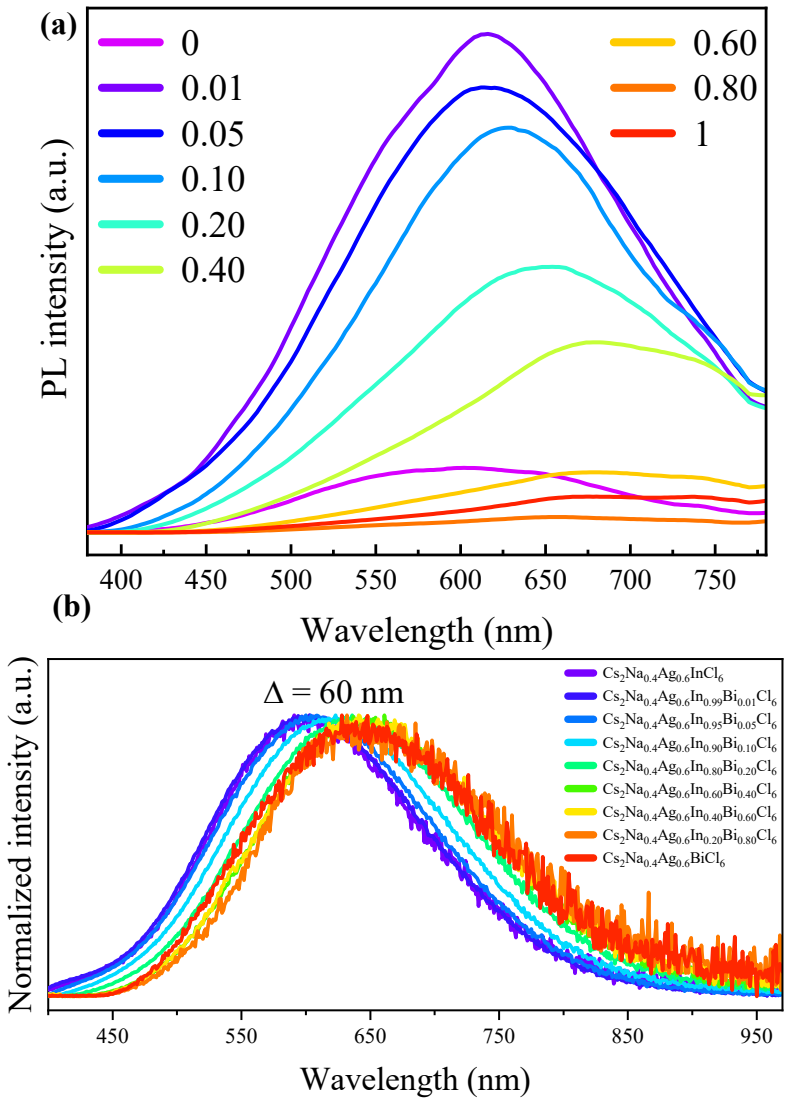

Figure S13. (a) Frequency-upconverted MPA PL spectra of $Cs_2Na_{0.4}Ag_{0.6}In_{1-x}Bi_xCl_6$ (x=0~1) DPs excited by 950 nm fs laser with pumping fluence of 120 mJ cm^{-2}. **(b)** Normalized single-photon PL spectra showing red-shifting of STE emission with increase of Bi^{3+} concentration.

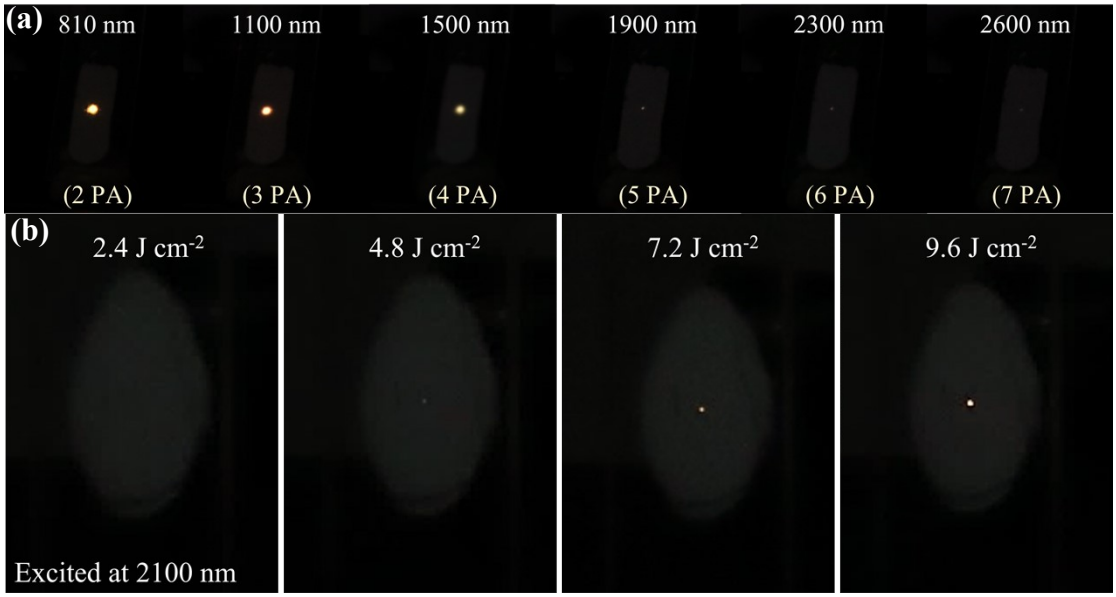

Figure S14. (a) MPA PL photographs of $Cs_2Na_{0.4}Ag_{0.6}In_{0.99}Bi_{0.01}Cl_6$ pumped by fs laser with different excitation wavelengths (810~2600 nm) and a fixed power density of 1.2 J cm^{-2}. **(b)** Six-photon upconverted emissive photographs pumped by fs laser (2100 nm) with various power densities.

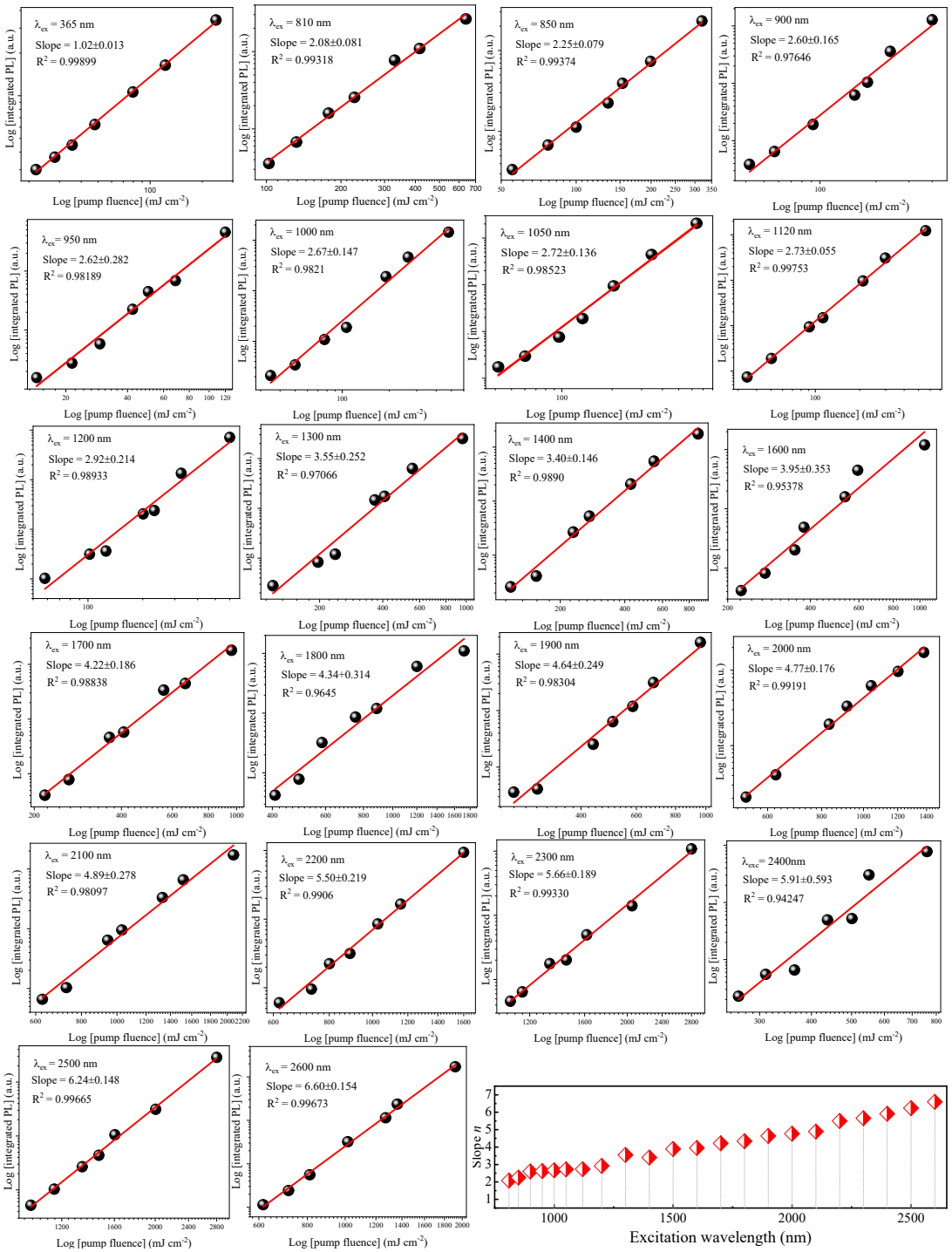

Figure S15. Log-log plots of integrated PL of $Cs_2Na_{0.4}Ag_{0.6}In_{0.99}Bi_{0.01}Cl_6$ in the excitation wavelength range of 365-2600 nm and the corresponding slope ***n*** value versus fs laser excitation wavelength.

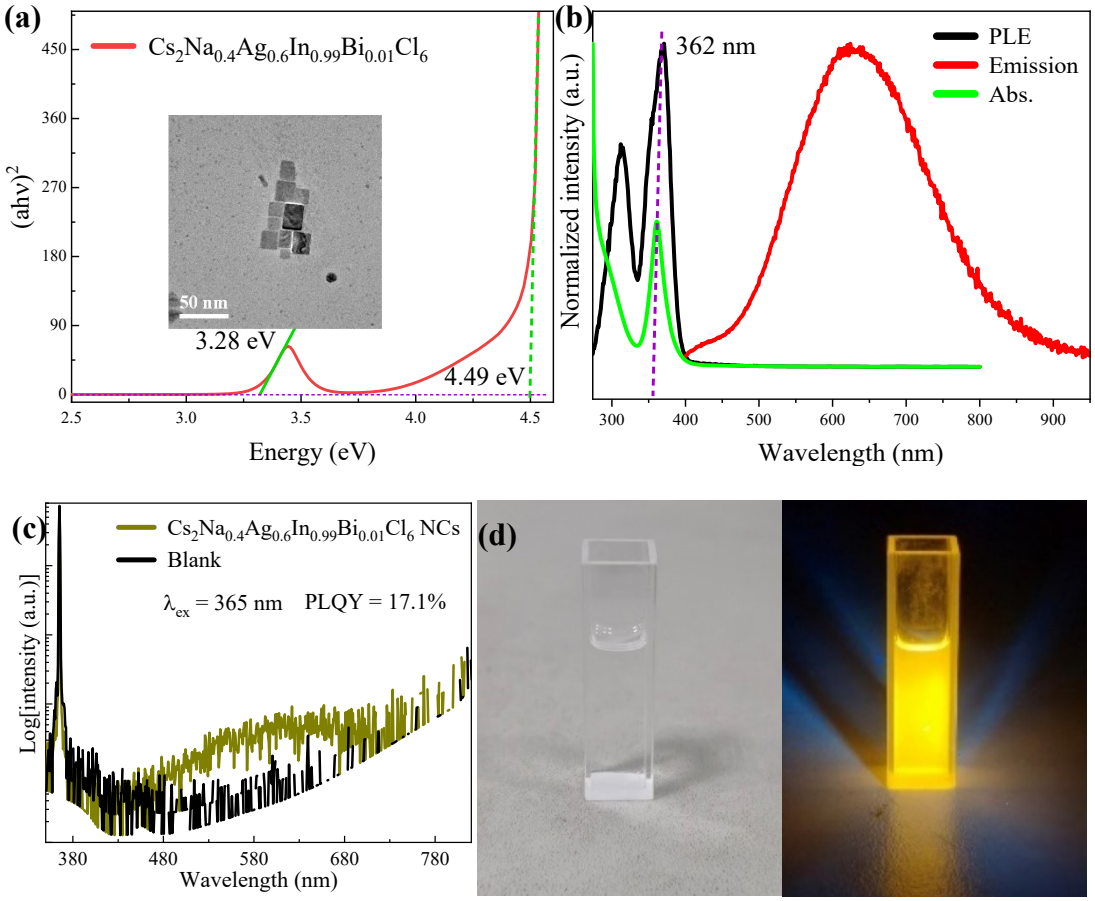

Figure S16. (a) Absorption, (b) PL, PLE spectra and (c) PLQY for the as-prepared $Cs_2Na_{0.4}Ag_{0.6}In_{0.99}Bi_{0.01}$ NCs. Inset is TEM image for the corresponding NCs. (d) Photographs of $Cs_2Na_{0.4}Ag_{0.6}In_{0.99}Bi_{0.01}$ colloidal solution under daylight and UV light irradiation, illustrating its high transparency and suitability for open-aperture Z-scan measurement.

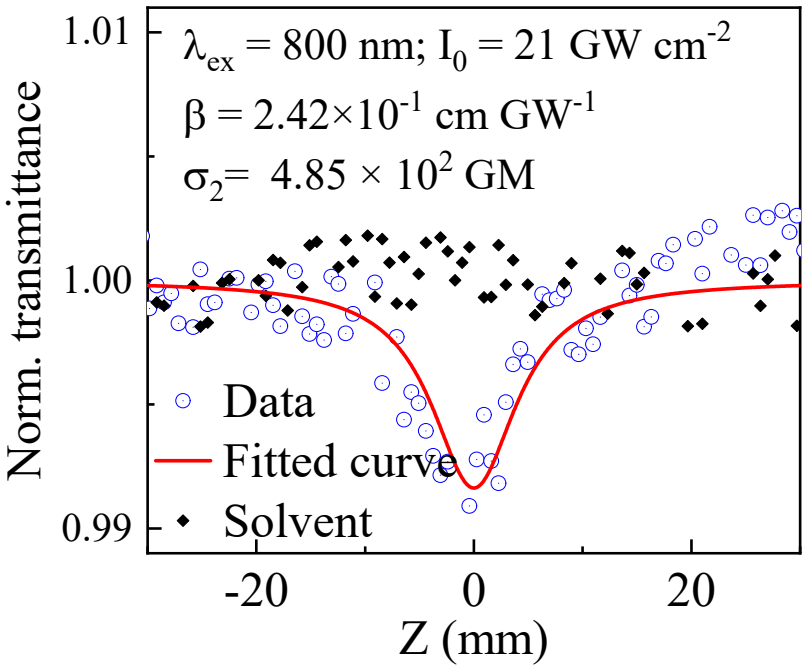

Figure S17. Open-aperture Z-scan results for $Cs_2Na_{0.4}Ag_{0.6}In_{0.99}Bi_{0.01}$ colloidal solution and blank hexane solvent at the excitation wavelength of 800 nm. The solid line is the fitting to the data using the Z-scan theory.

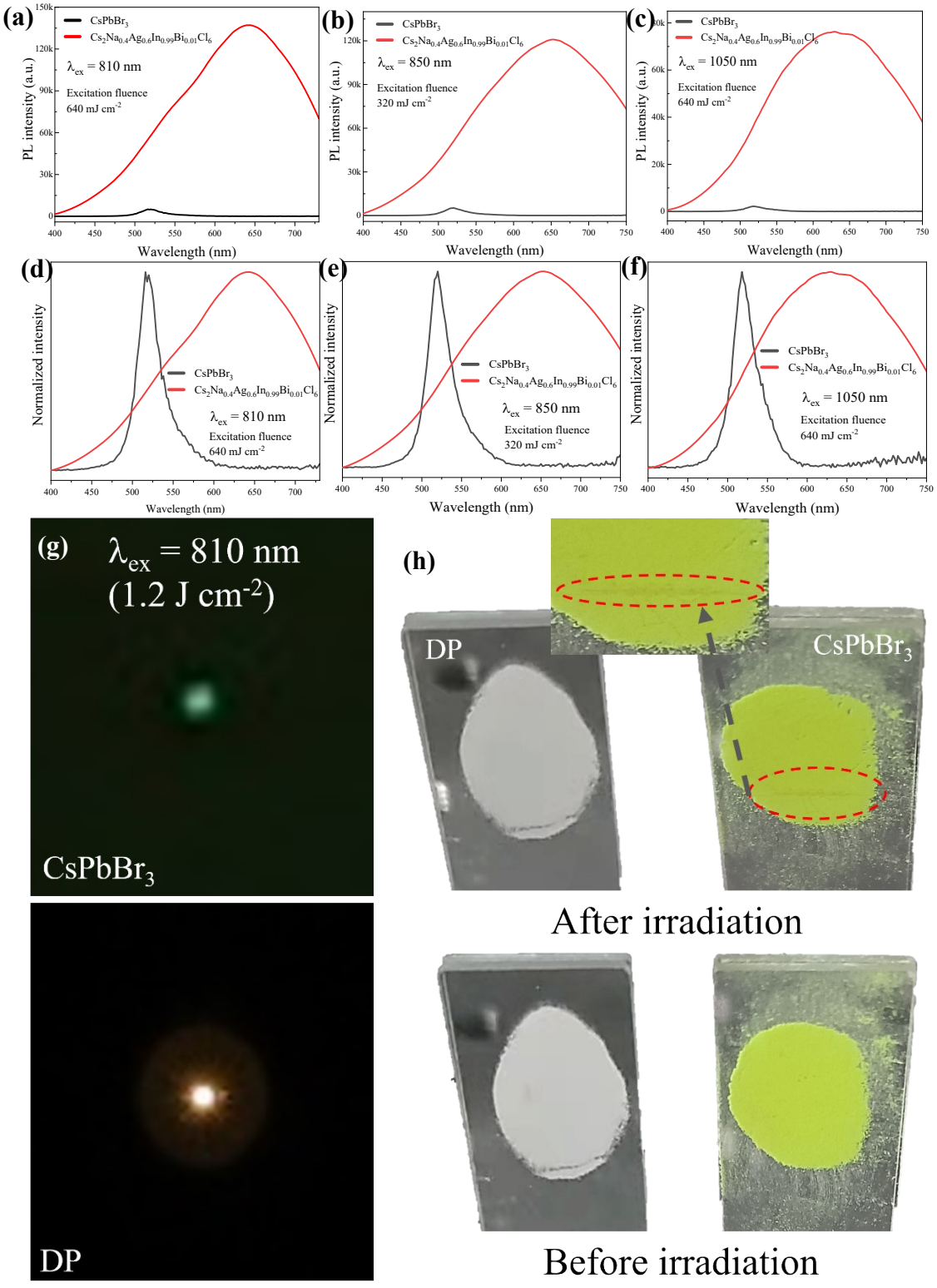

Figure S18. (a-f) MPA PL spectra from $CsPbBr_3$ LHP embedded glass (PLQY: 65%) and $Cs_2Na_{0.4}Ag_{0.6}In_{0.99}Bi_{0.01}Cl_6$ DP (PLQY: 99%) recorded under 810 nm, 850 and 1050 nm fs laser excitation and under the same experimental conditions. **(g)** Photographs of $CsPbBr_3$ LHP (top, green light) and $Cs_2Na_{0.4}Ag_{0.6}In_{0.99}Bi_{0.01}Cl_6$ DP

(bottom, yellow light) upon the 810 nm fs laser excitation with the same laser power (1.2 J cm^{-2}). **(h)** Stability test for $CsPbBr_3$ and $Cs_2Na_{0.4}Ag_{0.6}In_{0.99}Bi_{0.01}Cl_6$ via fs laser irradiation, showing that the former has obvious laser irradiation traces (red circle).

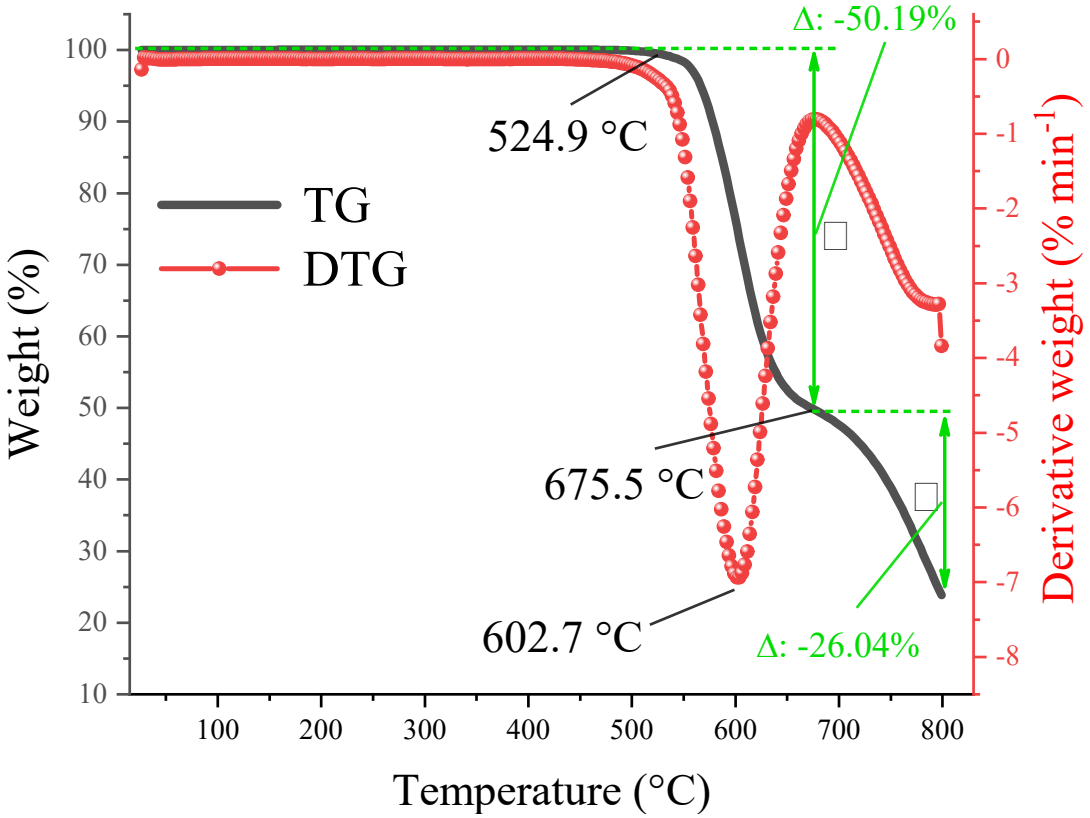

Figure S19. Thermogravimetric (TG) curve and derived thermogravimetry (DTG) curves of $Cs_2Na_{0.4}Ag_{0.6}In_{0.99}Bi_{0.01}Cl_6$ sample.

Note S2: TG curve (black) and DTG curve (red) measured for the DP in nitrogen starting from room temperature at a ramp rate of 10 °C min^{-1} to 800 °C. There is no change in mass from room temperature to 524.9 °C, indicating that the sample is stable during this temperature period. The temperature gradually increases to 800 °C, the weight loss phenomenon occurs in this stage and the temperature for the maximum weight loss is 602.7 °C.

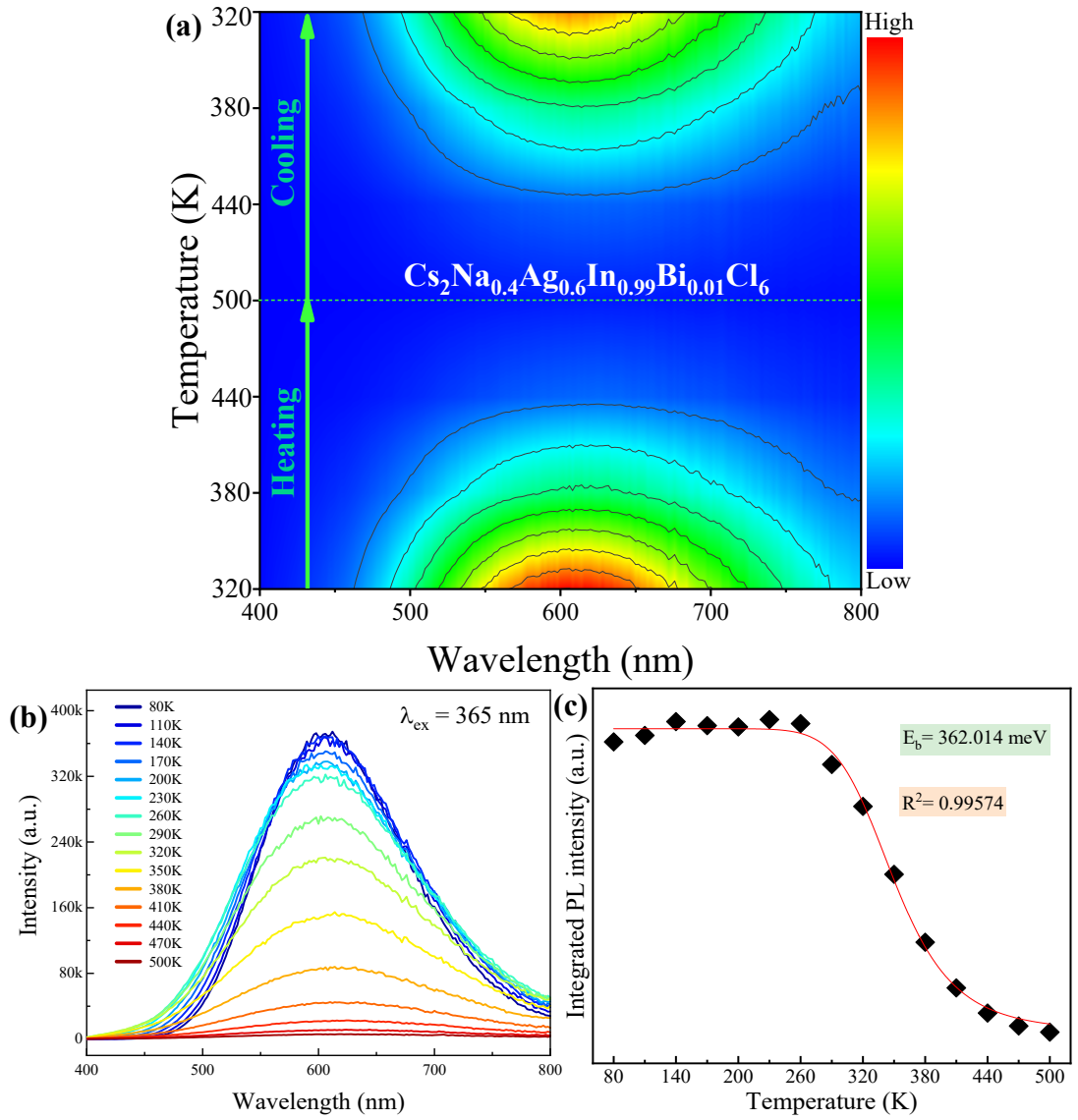

Figure S20. (a) PL spectra of $Cs_2Na_{0.4}Ag_{0.6}In_{0.99}Bi_{0.01}Cl_6$ recorded via a heating/cooling (80-500-80 K) cycle procedure. (b) PL spectra of DP sample recorded in a temperature range from 80 K to 500 K. (c) The evaluated exciton binding energy E_b by fitting the temperature dependent PL intensity.

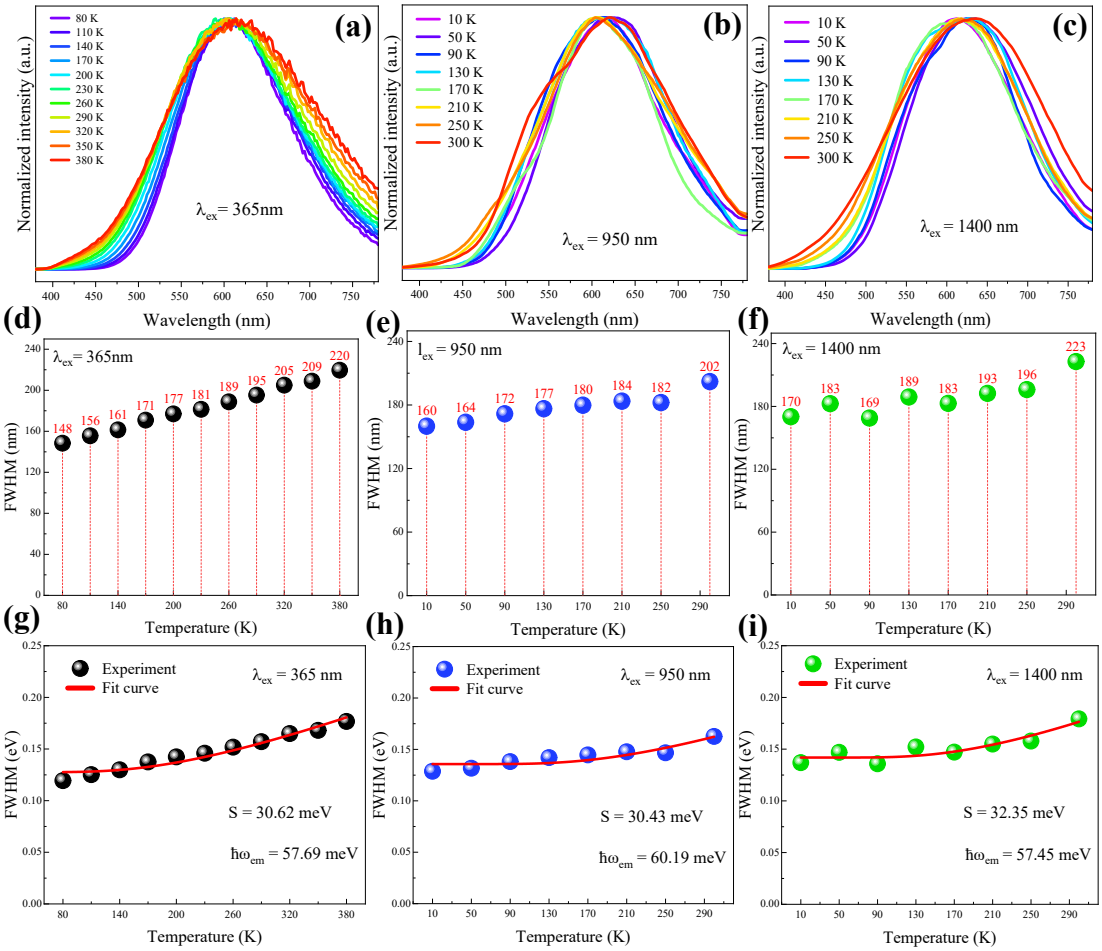

Figure S21. (a-c) Temperature dependent PL spectra and **(d-f)** FWHMs of $Cs_2Na_{0.4}Ag_{0.6}In_{0.99}Bi_{0.01}Cl_6$ DP under 365 nm, 950 nm, and 1400 nm laser excitation. **(g-i)** The fitted curves for the corresponding temperature-dependent FWHMs of DP recorded 365 nm, 950 nm, and 1400 nm laser excitation.

Note S3: Apparently, there is no significant change in the spectral profiles and FWHMs with elevation of temperature for the sample under single- and multi-photon absorption excitations, indicating that the higher-order MPA process does not cause obvious thermal effect. With elevation of temperature, FWHMs for both single- and multi-photon absorption excitation show a similar tendency of broadening. The temperature-dependent FWHMs can be fitted via the following equation:

$$FWHM(T) = 2.36\sqrt{S}\,\hbar\omega_{phonon}\sqrt{coth\frac{\hbar\omega_{phonon}}{2K_BT}}$$

where S is Huang-Rhys factor, $\hbar\omega$ is average phonon energy, K_B is Boltzmann constant and T is temperature. Accordingly, the Huang-Rhys factor and the average phonon energy are fitted to be

30.62 and 57.69 meV (λ_{ex} = 365 nm), 30.43 and 60.19 meV (λ_{ex} = 950 nm), 32.35 and 57.45 meV (λ_{ex} = 1400 nm), respectively, which indicates that the DP sample exhibit strong electron-phonon coupling for both linear and non-linear processes.

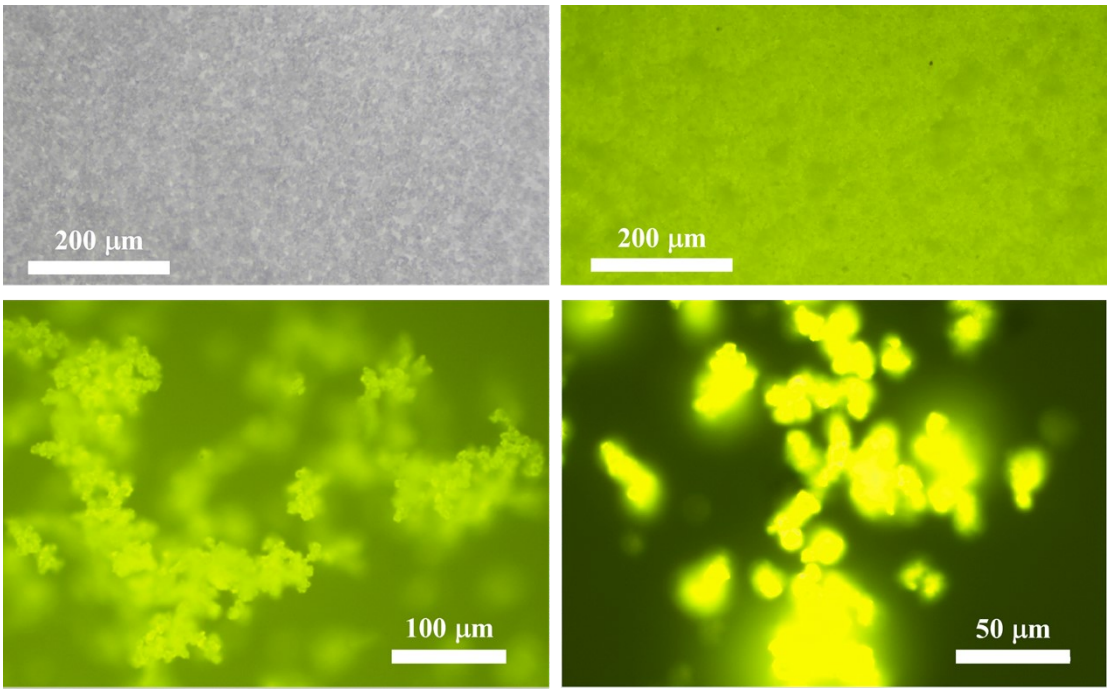

Figure S22. Fluorescence images of $Cs_2Na_{0.4}Ag_{0.6}In_{0.99}Bi_{0.01}Cl_6$ DP under 365 nm UV excitation.

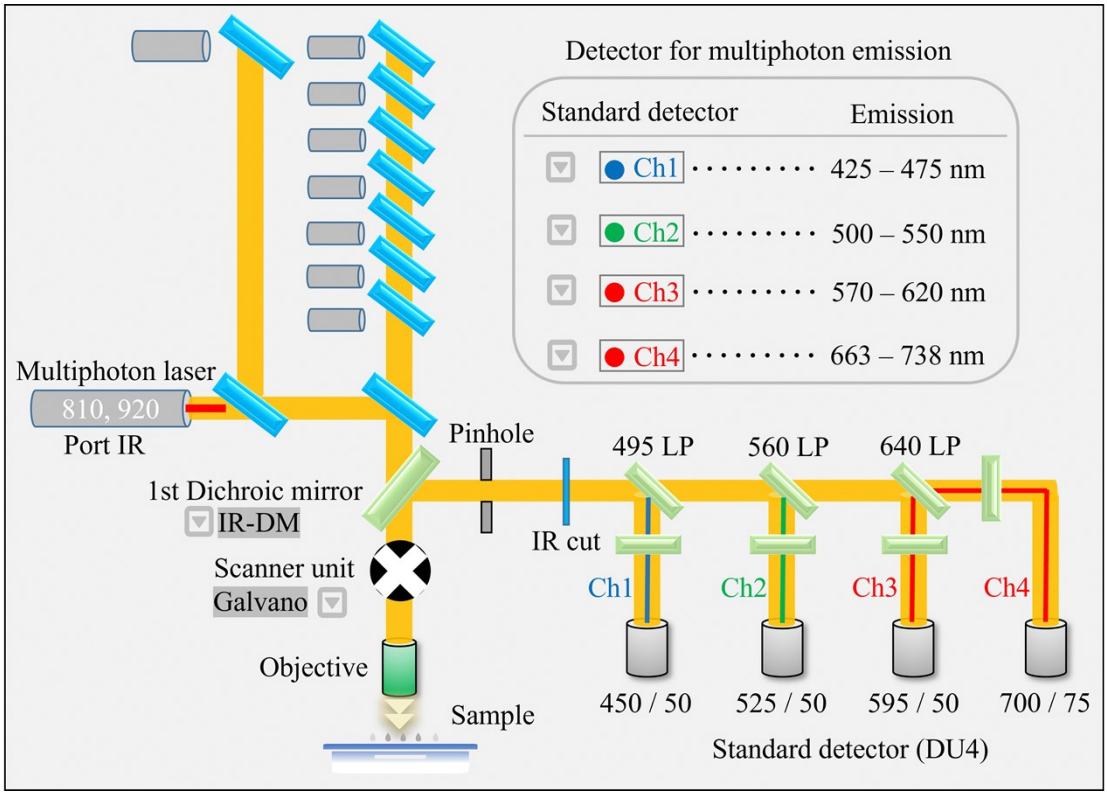

Figure S23. Schematic procedure for recording multi-photon imaging. A femtosecond laser beam excites the DP sample through a series of lens and dichroic mirrors, and the images can be collected and overlapped with the help of four standard detector channels.

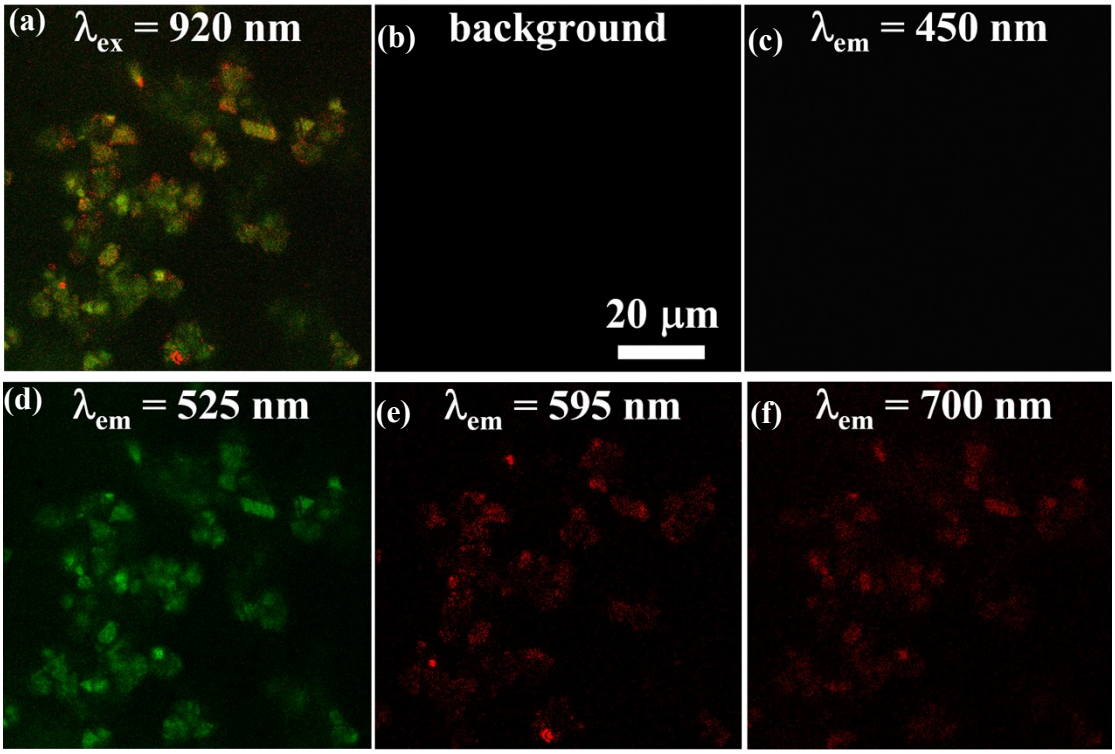

Figure S24. (a) Three-photon fluorescence imaging of $Cs_2Na_{0.4}Ag_{0.6}In_{0.99}Bi_{0.01}Cl_6$ upon 920 nm fs laser excitation, where the combined fluorescence is collected from **(b)** background, **(c)** 425 - 475 nm, **(d)** 500 - 550 nm, **(e)** 570 - 620 nm and **(f)** 663 - 738 nm emissions.

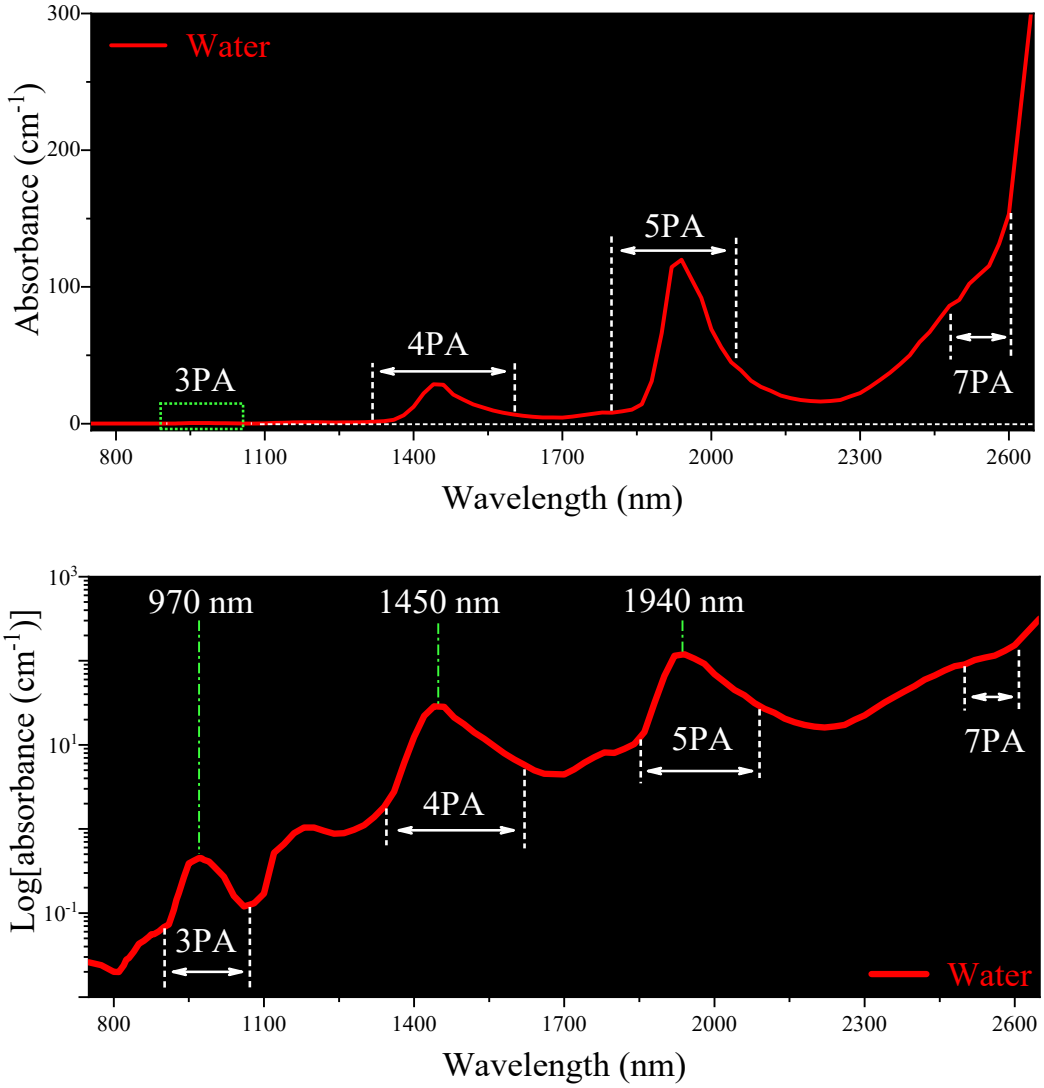

Figure S25. Absorption spectrum of water, showing strong absorptions in several specific spectral positions for 3PA-7PA processes.

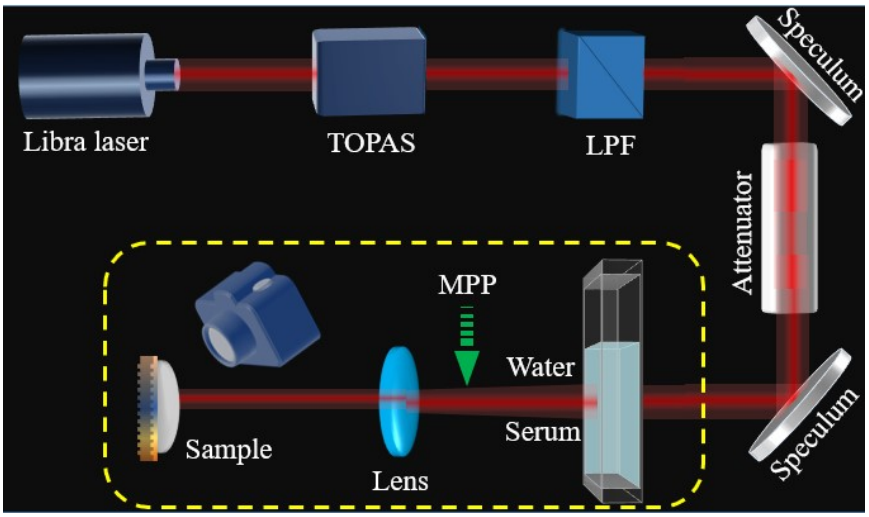

Figure S26. Light path diagram to record MPA imaging pumped by fs laser passing through water or serum. LPF and MPP represents long-pass filter and measuring power position, respectively.

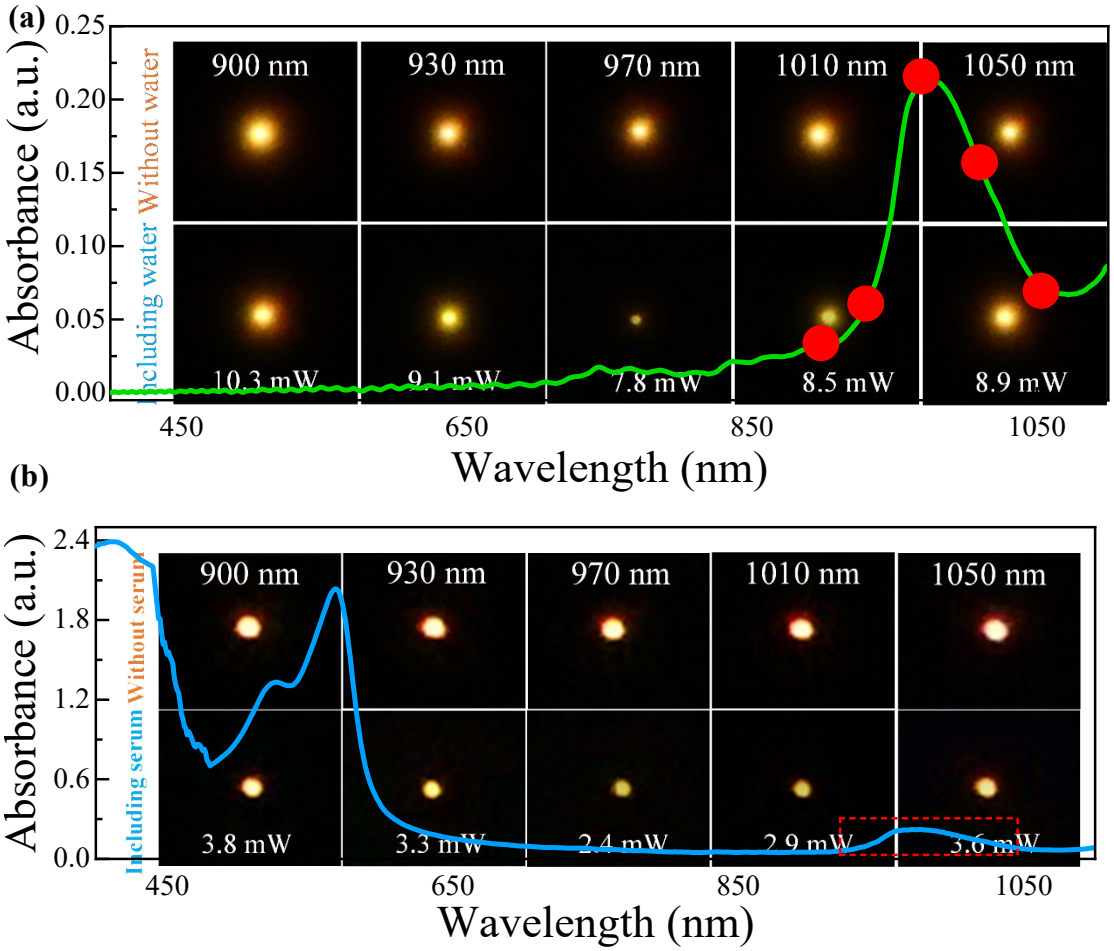

Figure S27. 3PA imaging pumped by fs laser passing through (a) water and (b) serum. Different fs laser pumping wavelengths are indexed in the figure, and the background is the absorption of water and serum related to the spectral range for the 3PA processes. As a reference, 3PA imaging pumped by fs laser without passing through water and serum is provided. The measured 3PA emitting powers are also given in the figure.

References

S1. W. Chen, S. Bhaumik, S. A. Veldhuis, G. Xing, Q. Xu, M. Grätzel, S. Mhaisalkar, N. Mathews and T. C. Sum, *Nat. Commun.*, 2017, **8**, 1-9.

S2. A. Manzi, Y. Tong, J. Feucht, E. P. Yao, L. Polavarapu, A. S. Urban and J. Feldmann, *Nat. Commun.*, 2018, **9**, 1-6.

S3. D. Yang, S. Chu, Y. Wang, C. K. Siu, S. Pan and S. F. Yu, *Opt. Lett.*, 2018, **43**, 2066-2069.

S4. K. Krishnakanth, S. Seth, A. Samanta and S. V. Rao, *Nanoscale*, 2019, **11**, 945-954.

S5. J. Li, F. Zhao, S. Xiao, J. Cheng, X. Qiu, X. Lin, R. Chen and T. He, *Opt. Lett.*, 2019, **44**, 3873-3876.

S6. G. Walters, B. R. Sutherland, S. Hoogland, D. Shi, R. Comin, D. P. Sellan, O. M. Bakr and E. H. Sargent, *ACS Nano*, 2015, **9**, 9340-9346.

S7. T. He, J. Li, C. Ren, S. Xiao, Y. Li, R. Chen and X. Lin, *Appl. Phys. Lett.*, 2017, **111**, 211105.

S8. L. Zhang, M. Morshedi and M. G. Humphrey, *Angew. Chem. Int. Ed.*, 2022, **61**, e202116181.

S9. B. Zhao, X. Jia, J. Liu, X. Ma, H. Zhang, X. Wang and T. Wang, *Ind. Eng. Chem. Res.*, 2016, **55**, 1801-1807.

S10. P. L. Wu, X. J. Feng, H. L. Tam, M. S. Wong and K. W. Cheah, *J. Am. Chem. Soc.*, 2009, **131**, 886-887.

S11. S. C. Pu, M. J. Yang, C. C. Hsu, C. W. Lai, C. C. Hsieh, S. H. Lin, Y. M. Cheng and P. T. Chou, *Small*, 2006, **2**, 1308-1313.

S12. J. W. Chon, M. Gu, C. Bullen and P. Mulvaney, *Appl. Phys. Lett.*, 2004, **84**, 4472-4474.

S13. Z. Guo, J. Li, Y. Gao, J. Cheng, W. Zhang, R. Pan, R. Chen and T. He, *J. Mater. Chem. C*, 2020, **8**, 16923-16929.

S14. C. Kriso, M. Stein, T. Haeger, N. Pourdavoud, M. Gerhard, A. Rahimi-Iman and T. Riedl, M. Koch, *Opt. Lett.*, 2020, **45**, 2431-2434.

S15. A. Mushtaq, D. Kushavah, S. Ghosh and S. K. Pal, *Appl. Phys. Lett.*, 2019, **114**, 051902.

S16. D. Wawrzynczyk, J. Szeremeta, M. Samoc and M. Nyk, *APL Mater.*, 2015, **3**, 116108.

S17. L. Yang, K. Wei, Z. Xu, F. Li, R. Chen, X. Zheng, X. Cheng and T. Jiang, *Opt. Lett.* 2018, **43**, 122-125.

S18. W. Meng, X. Wang, Z. Xiao, J. Wang, D. B. Mitzi and Y. Yan, *J. Phys. Chem. Lett.*, 2017, **8**, 2999-3007.